Earthquake Geotechnical Engineering for Protection and Development of Environment and Constructions – Silvestri & Moraci (Eds)
© 2019 Associazione Geotecnica Italiana, Rome, Italy, ISBN 978-0-367-14328-2

Numerical study on seismic behavior of a piled raft foundation with grid-form DMWs considering post-peak softening of stabilized soil

Y. Shigeno, K. Yamashita & J. Hamada
Takenaka R&D Institute, Takenaka Corporation, Inzai, Chiba, Japan

ABSTRACT: This paper describes the seismic performance of a piled raft foundation combined with grid-form deep mixing walls considering the tensile and shear strength and the post-peak softening of stabilized soil. A 12-story building was modeled using a three-dimensional finite element soil–structure interaction model. The model was calibrated in a previous study with the seismic observation records of a middle-scale earthquake at the building site. An elasto–plastic model with tensile and shear criteria that can describe post-peak softening is used for the stabilized soil. The analysis result obtained under a strong earthquake input motion indicates that the induced stress reaches the tensile strength in some parts of the deep mixing walls. However, few parts lose tensile strength as a result of post-peak softening, and the grid-form deep mixing walls are found to successfully reduce the bending moment of the piles to an acceptable level.

1 INTRODUCTION

In recent years, piled raft foundations have been used even on liquefiable sand by adding grid-form cement deep mixing walls (DMWs) (Yamashita et al. 2016). Grid-form DMWs work not only as a countermeasure against liquefaction but also as a part of foundation. However the seismic behavior of this foundation is not well understood because of its complexity. The seismic behavior of this foundation has been studied by the numerical simulation of the field observation records (Yamashita et al. 2012, 2018, Shigeno et al. 2017). And the soundness of the piles was confirmed even though the grid-form DMWs were partially failed under strong earthquakes. However, the softening of the DMWs was not considered despite the fact that they are known to undergo post-peak softening. Thus in the present study, an elasto-plastic model that is able to describe the post-peak softening was applied to DMWs. This paper mainly discusses the effect of the softening of the DMWs on the sectional force of the piles.

2 OVERVIEW OF BUILDING AND GROUND

Figure 1 shows a schematic view of the building and its foundation with the soil profile. The analyzed building is a 12-story reinforced-concrete building with a seismic base-isolation system located in Tokyo. The soil down to a depth of 44 m is very soft alluvial strata composed mainly of silty clay. The strata deeper than 44 m are diluvial sand and a gravel layer with SPT N-value of 60 or higher. The ground water table is approximately 1.8 m below the ground surface. The building is supported by a piled raft with grid-form DMWs which were employed to prevent the liquefaction of the silty sand from GL –3 m to –7 m as well as to improve the bearing capacity of the raft foundation. The spacing between the DMWs is approximately 6–9 m, and the area replacement ratio is 25%. At the time of the 2011 off the Pacific coast of Tohoku earthquake, the seismic response of the soil-foundation system and the accelerations of the ground and structure were successfully recorded (Yamashita et al. 2012).

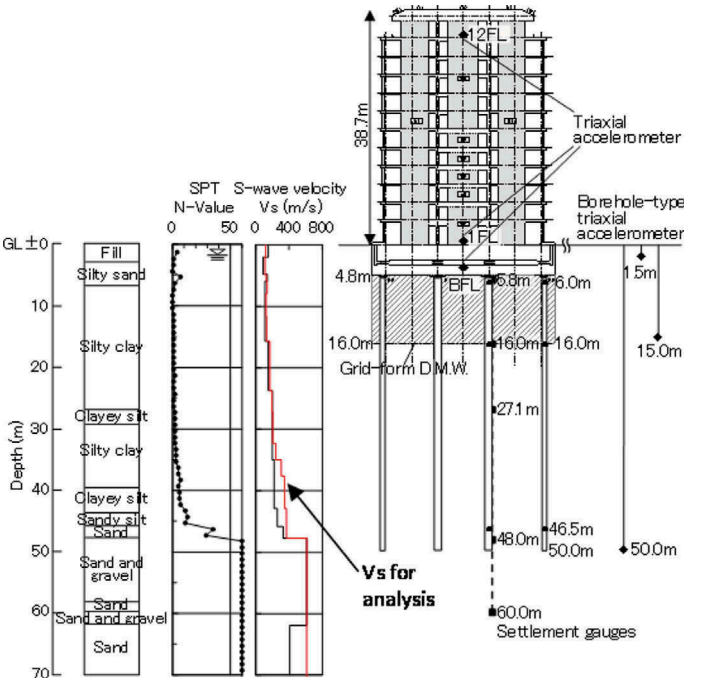

Figure 1. Schematic view of building, soil profile and monitoring devices.

3 ANALYSIS MODEL

3.1 *Finite element mesh*

Figure 2(a) shows the finite element (FE) mesh, which consists of 213,622 elements. The superstructure was modeled using elastic bars and shells, and the piles were modeled by elastic bars. The upper 12 m of the piles are SC piles, and the lower 33 m are PHC piles, with diameters from 0.8 to 1.2 m. The raft was modeled using elastic solids. Rayleigh damping was applied to these components at a damping ratio of 2%. Figure 2(b) shows a top-down view of the FE mesh beneath the raft. Cavities were made in the shape of the piles, and the nodes of the piles and the ground at the same depth were bound by rigid bars. The base isolation system was modeled

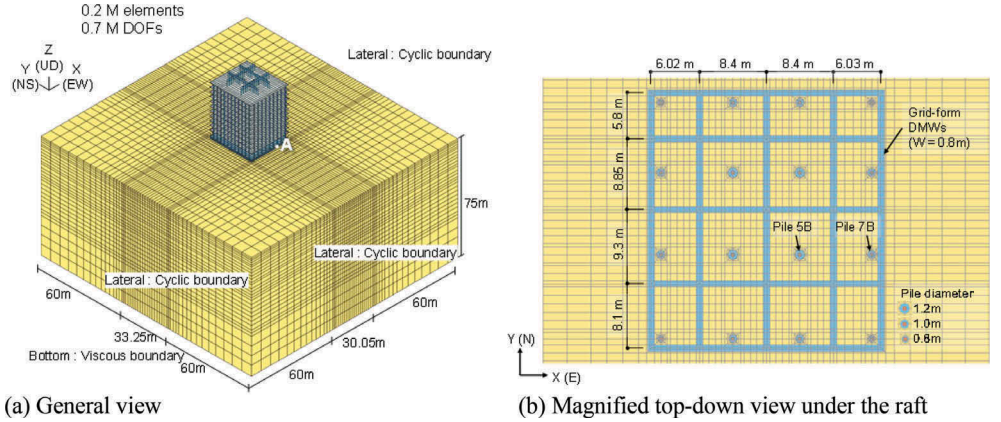

(a) General view (b) Magnified top-down view under the raft

Figure 2. Finite element model.

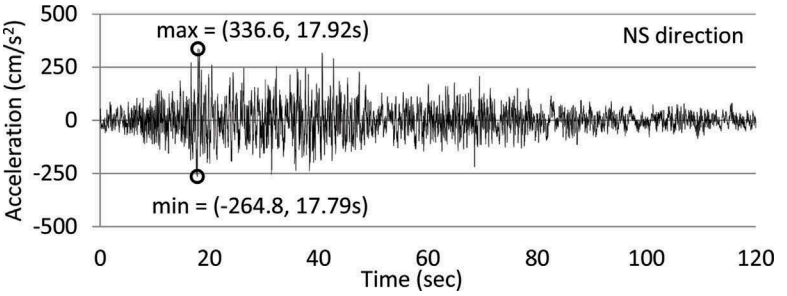

Figure 3. Input acceleration wave at a depth of 75 m (2E : twice of the incident wave) in the NS direction

using a tri-linear spring. The lateral boundaries were periodic boundaries. The bottom was a viscous boundary. The software is an in-house program called MuDIAN (Shiomi et al. 1998).

3.2 *Input motion*

An artificial wave was used for a strong earthquake called 'Level 2 earthquake' that is officially notified in Japanese building design code. The wave is defined by an acceleration response spectrum with a peak of 800 Gal from 0.16 to 0.64 s. The input wave was generated using the phase data of the 1968 Tokachi-oki Earthquake at Hachinohe Bay. The NS directional input motion was applied. Figure 3 shows the input motion, and the maximum acceleration is 337 Gal.

3.3 *Soil model*

The Yoshida model for multiple-dimensions (Tsujino et al. 1994) was used for the soil. The Yoshida model is a two-surface nonlinear elastic model and is characterized using G–γ and h–γ characteristics directly as input data. The profile of the shear wave velocity for the analysis is shown in Figure 1 as a red line. The profile was obtained by calibration analysis using the observed records (Shigeno et al. 2017). Liquefaction was not considered in this study.

3.4 *Constitutive model for stabilized soil*

The model proposed by Namikawa et al. (2007) was used for the stabilized soil. The model has three characteristics. (1) Two different failure criteria are employed for tensile and shear failure. (2) Strain-softening is considered after the peak strength. (3) The smeared crack concept is used in the strain-softening rules.

The tensile criterion considering softening using the damage parameter ω is expressed as Equation 1 below (note that tension is positive):

$$\frac{2\left(J'_2\right)^{\frac{1}{2}}}{\sqrt{3}}\sin\left(\theta+\frac{2\pi}{3}\right)+\sigma_m = T_f(1-\omega) \tag{1}$$

Where J'_2 is the second invariant of deviatoric stress, θ is the Lode angle, σ_m is mean stress, T_f is the tensile strength, ω is the damage parameter.

The damage parameter ω for tensile failure is expressed as a function of the maximum plastic principal strain $\varepsilon_1{}^{\mathrm{p}}$ using a 1/4 bilinear model obtained by analyzing the bending test of the stabilized beam.

$$\begin{aligned}\omega &= l_m\frac{T_f}{G_f}\left(\varepsilon_1^p-\varepsilon_{1peak}^p\right)\ \ \omega\le 0.75\\ \omega &= \frac{12}{17}-\frac{1}{17}l_m\frac{T_f}{G_f}\left(\varepsilon_1^p-\varepsilon_{1peak}^p\right)\ \ 0.75<\omega\le 1.0\end{aligned} \tag{2}$$

Where, G_f is the fracture energy, $\varepsilon_1{}^p{}_{peak}$ is the peak plastic principal strain and l_m is a parameter that depends on the mesh size of the finite element model. The parameter l_m is introduced to remove the mesh size dependency of the strain localization.

The shear criterion is based on the Mohr–Coulomb criterion. The yielding function considering strain-hardening and softening is expressed as Equation 3 below:

$$\left(J_2'\right)^{\frac{1}{2}} + \left(\frac{\sqrt{3}\sin\varphi}{\sqrt{3}\cos\theta - \sin\theta\sin\varphi}\right)\left\{\sigma_m - \frac{c(1-\omega)}{\tan\varphi}\right\}k_y = 0 \tag{3}$$

Where c is the cohesion, ϕ is the friction angle, k_y is an internal state variable describe the hardening. The variable k_y determines the loading surface size, and it is assumed to be the hyperbolic function of the second invariant of the deviatoric plastic strain $\bar{\varepsilon}^p$ as Equation 4 below:

$$\frac{k_y - k_0}{k_f - k_0} = \frac{\frac{\bar{\varepsilon}^p}{e_y}}{1 + \frac{\bar{\varepsilon}^p}{e_y}} \qquad k_0 = \frac{T_f}{\sigma_m - \frac{ac}{\tan\phi}} \tag{4}$$

Where k_f is the coefficient of the normal-yield surface, e_y and α are hardening parameters.

From the experimental results, the damage parameter ω for shear was assumed as Equation 5.

$$\omega = 1 - \exp\left\{-\frac{R_l\left(\bar{\varepsilon}^p - \bar{\varepsilon}^p_{peak}\right)}{e_r}\right\} \qquad R_l = \frac{l_m}{l_c} \tag{5}$$

Where l_c is the characteristic length that specifies the size of the failure region, and e_r is the material parameter. The damage parameter ω is common to both the tensile and shear criterion, and the loading surface reduces in both criteria after the stress reaches the strength. Figure 4 shows the two failure criteria of the model and how they reduce by softening.

The Building Center of Japan (BCJ) (2002) has proposed that the design standard compressive strength F_c of the stabilized soil is to be set 1.3 standard deviations below the average compressive strength of in-situ core samples. From 36 core samples aged 28 days, F_c was set to 2.6 MPa (Yamashita et al. 2015). The other parameters were also adopted the BCJ proposal as shown in Table 1. The initial shear modulus G_0 was determined from the calibration analysis of the observation records of the 2011 off the Pacific coast of Tohoku earthquake (Shigeno et al. 2017). As for the initial stress in the DMWs, an isotropic stress of 170 kPa was applied based on the measured vertical pressure 300 kPa between the raft and the DMWs (Yamashita et al. 2015) and the horizontal stress calculated using the coefficient of earth

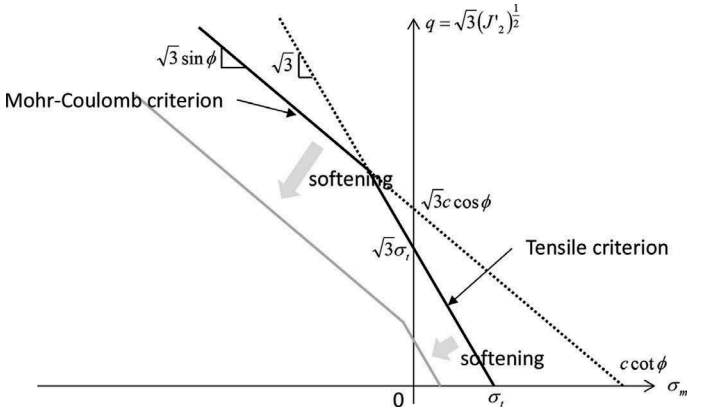

Figure 4. Criteria of Namikawa model (tension is positive)

Table 1. Strength parameters of the stabilized soil

Compressive strength	F_c	MPa	2.60
Tensile strength	$0.2F_c$	kPa	520
Cohesion	$0.3F_c$	kPa	780
Friction angle	ϕ	degree	30
Poisson's ration	v		0.26
Density	ρ	t/m^3	2.00
Initial shear modulus	G_0	MPa	500

Table 2. Parameters of the Namikawa model

Hardening parameter	α		0.9
Hardening parameter	e_y		0.0001
Fracture energy	G_f	N/m	96.0
Softening parameter for shear	e_r		0.4
Dilatancy coefficient	D_c		0.0
Localization size	l_m	mm	1000
Characteristics length	l_c	mm	0.6

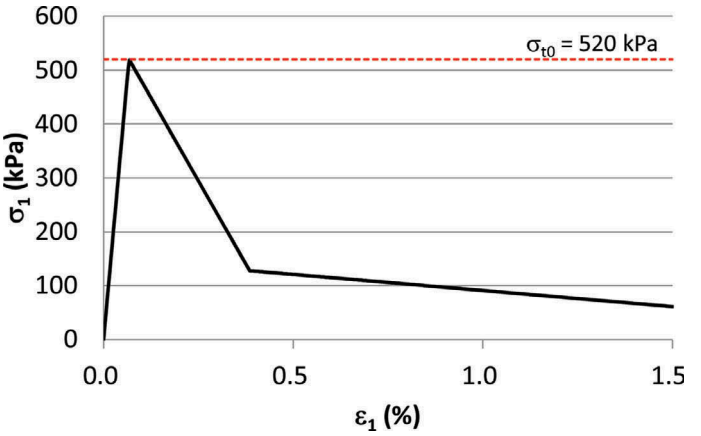

Figure 5. Results of numerical uniaxial extension test of stabilized soil

pressure at rest. The properties and parameters of the Namikawa model were set in reference to Namikawa (2006) as given in Table 2. Stiffness proportional damping of 5% was applied to the DMWs considering the previous study (Yamashita et al. 2018) and no strain-hardening assumption for the tensile criterion.

Figure 5 shows the simulation result of the uniaxial extension test. Where σ_1 is the maximum principal stress, and ε_1 is the maximum principal strain. The properties given in Tables 1 and 2 were used. The initial stress was zero, and the extension was applied under strain-constrained condition. The stress degraded after it reached the initial tensile strength σ_{t0} = 520 kPa.

4 RESULTS

The case without DMWs was also analyzed to clarify their effect. Figure 6(a) shows the profiles of the peak acceleration at the center of the superstructure and the raft together with the ground at point A (Figure 2(a)). The peak acceleration profile of the soil column model ("Free Field") is also plotted by the blue line. The PGA at the surface of the soil column was 296 Gal. In the case with DMWs, the peaks were 272 Gal at the raft and 130 Gal on the first

floor. The peaks of the raft are similar in both cases. Figure 6(b) shows the profiles of the peak displacement relative to GL –49.9 m. The peak displacements of the raft were –10.8 and 8.0 cm with DMWs, and –15.7 and 10.1 cm without DMWs. Thus, the ground deformation beneath the raft was reduced by the DMWs, and this affects the sectional force of the piles.

Figure 7 illustrates the extent of the tensile failure in the grid-form DMWs during the earthquake in two different angled view from above. The elements are colored according to the number of Gauss points where the induced stress reached the tensile strength. The number of Gauss points in each element is eight, and then the maximum value is 8. Tensile failure occurred mostly in the lower part of the longitudinal walls, which lie parallel to the shaking direction, and this is due to shear deformation. In the upper part of the longitudinal walls, few tensile failure elements were observed because the deformation was restricted by the raft. In the transverse walls, some elements at the bottom of the grid crossing corners failed due to bending.

Figure 8 shows the residual tensile strength of the each element at the final time step. As shown in this figure, some elements completely lost their tensile strength. However, most of the elements maintained a high tensile strength, despite the stress of some reaching the tensile strength as shown in Figure 7.

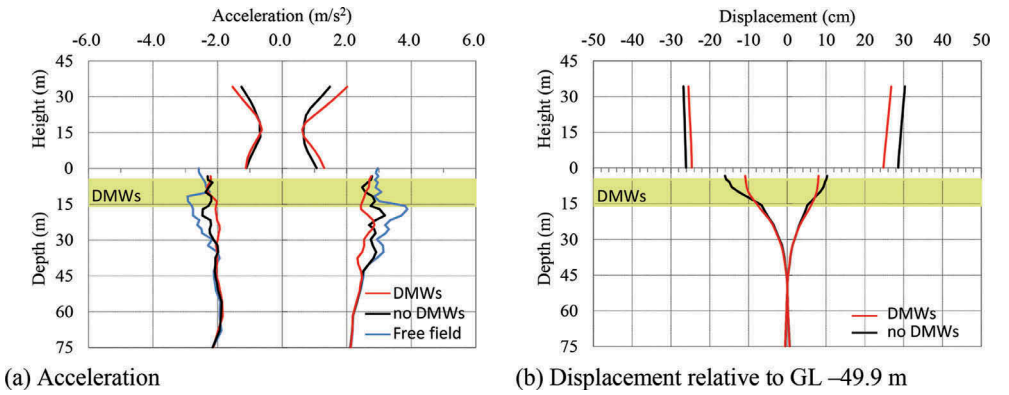

Figure 6. Peak response profiles of the center of the superstructure and the ground at point A (NS-direction).

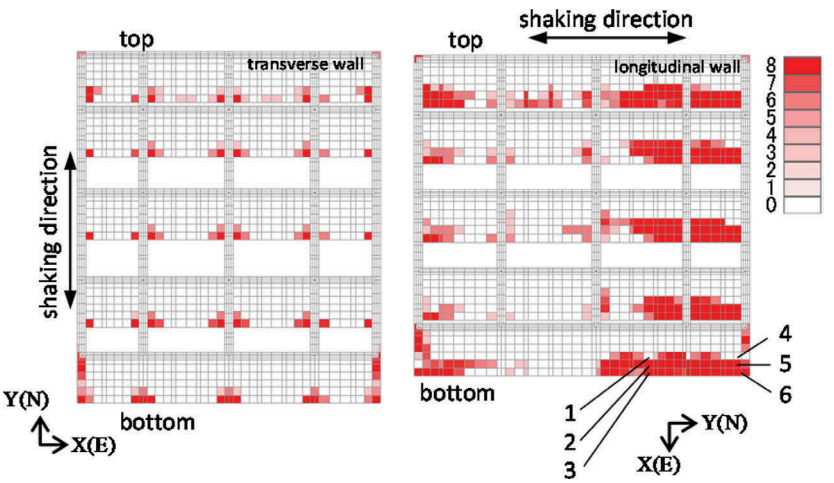

Figure 7. Color map of the number of tensile failure Gauss points in grid-form DMWs (two angled views from above).

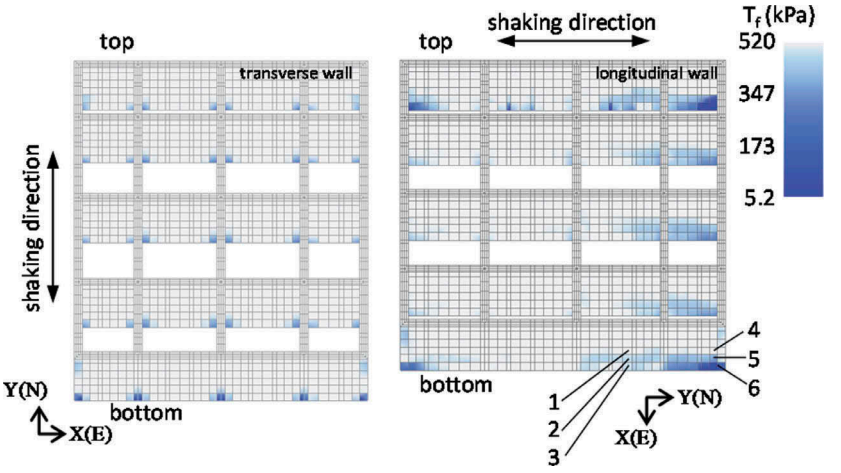

Figure 8. Color map of residual tensile strength at the final step (two angled views from above).

Figure 9 shows the time histories of the tensile strength of the elements labeled in Figures 7 and 8. The red dot line is the initial tensile strength σ_{t0} = 520 kPa. In elements 1 and 4, tensile failure did not occur as shown in Figure 7, nor did softening. In elements 2 and 3, the stress reached the tensile strength at all of the Gauss points. However, the residual strength of these elements was approximately 90% of the initial value, and remained stable over time. All of the Gauss points also failed in elements 5 and 6. In element 5, the residual strength ratio was 64%. And in element 6, the tensile strength degraded to 1% of the initial strength which was the limitation value given as a parameter. Significant softening was localized at the lower corner of the outermost part of the grid-form DMWs. These results show that intensely colored regions in Figure 7 do not represent the parts where the strength is completely degraded. It is important to note that the elements maintained a relatively high residual strength even though the all of the Gauss points failed by tension.

Figure 10 shows the profiles of the peak bending moment in piles 5B and 7B (see Figure 2(b)). The moment near the pile head in the case with DMWs was remarkably smaller than that in the case without DMWs. In the case with DMWs, the deformation of the soil enclosed by

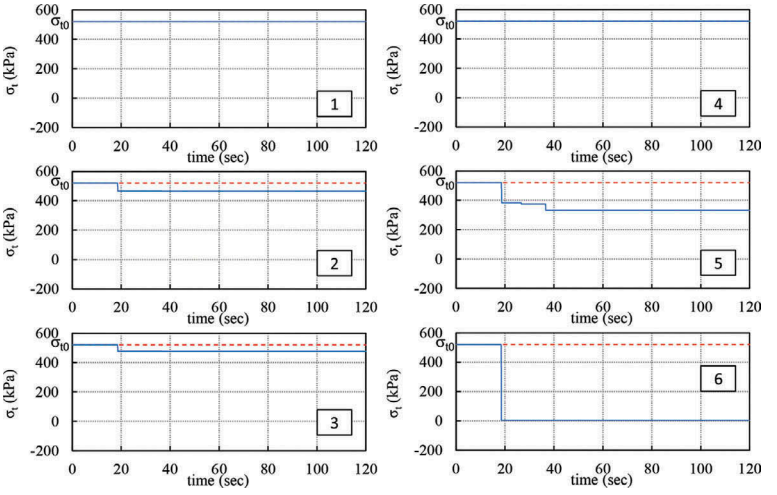

Figure 9. Time histories of tensile strength

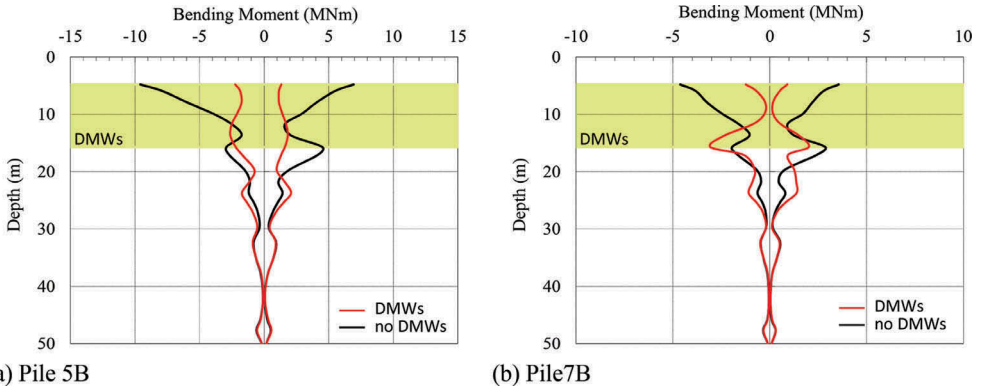

Figure 10. Profiles of peak bending moment of piles.

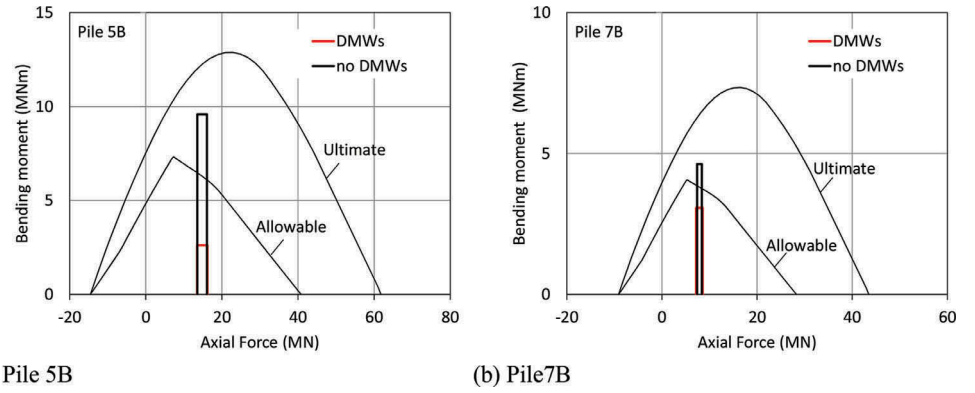

Figure 11. Calculated maximum moment along the pile and the design N–M interaction curves of SC piles.

the DMWs was small and resulted in a small bending moment near the pile head. However, the moment at the bottom of the DMWs was large, because the high rigidity of the DMWs at this point produced a large curvature displacement. In contrast, in the case without DMWs, the deformation of the soil near the pile head was large and asymmetric in the peak profile. This results in a large and asymmetric bending moment at the pile head. These results show the same tendency as the case without softening of the DMWs (Yamashita et al. 2018).

Figure 11 shows the relationship between the axial force and the bending moment of piles 5B and 7B, with the design interaction curves of the steel pipe–concrete composite (SC) piles (Japan Pile Corporation 2011) that were used upper 12 m. The axial force is the sum of the statically measured pile head load and the dynamic increment in the analysis, and the bending moment is the maximum value along the SC pile. The results show that the maximum bending moments with DMWs were below the allowable criterion. In contrast, the maximum bending moments without DMWs were close to the ultimate criterion. This shows that the DMWs are quite effective at reducing pile bending moment to an acceptable level, although the induced stress in the DMWs partially reached the tensile strength and softened under a strong earthquake load.

5 CONCLUDING REMARKS

The seismic response analysis of a piled raft foundation with grid-form DMWs was carried out using a three-dimensional nonlinear finite element model under a strong earthquake load

considering the post-peak softening of the DMWs. As a result, the induced stress reached the tensile strength and softening occurred in some lower parts of the DMWs. However, the bulk of the DMWs maintained a high tensile strength, and the DMWs were still able to reduce the bending moment of the piles to an acceptable level. This indicates that grid-form DMWs can be designed more rationally by applying a performance-based design method in which a partial failure of the DMWs is accepted. To verify the numerical analysis results, further study based on physical modeling such as using a geotechnical centrifuge would be required.

REFERENCES

Building Center of Japan, 2002. *Specification for design and quality control of cement treated soil* (in Japanese).

Japan pile corporation, 2011. *Pile foundation design materials* (in Japanese)

Namikawa, T. & Koseki, J. 2006. Experimental determination of softening relations for cement-treated sand. *Soils & Foundations* 46(4): 491–504.

Namikawa, T. & Mihira, S. 2007. Elasto-plastic model for cement-treated sand. *Int. J. Numer. Anal. Mech. Geomech*. 31: 71–107.

Shigeno, Y., Yamashita, K., Hamada, J. & Nakamura, N. 2017. Numerical evaluation of seismic performance of piled raft with grid-form DMWs under large earthquake loads, *Design and analysis of pile raft foundations -2017*, 109–127, Taipei: Tamkang University Press.

Shiomi, T., Shigeno, Y. & Zienkiewicz, O. C., 1993. Numerical prediction for model No. 1., *Verification of Numerical Procedures for the Analysis of Soil Liquefaction Problems* (ed. by Arulanandan & Scott), 213–219, Balkema.

Tsujino, S., Yoshida, N. & Yasuda, S. 1994. A simplified practical stress-strain model in multi-dimensional analysis, *Proc. of International Symposium on Pre-failure Deformation Characteristics of Geomaterials*, Sapporo, 463–468.

Yamashita, K., Hamada, J., Onimaru, S. & Higashino, M. 2012. Seismic behavior of piled raft with ground improvement supporting a base-isolated building on soft ground in Tokyo. *Soils & Foundations* 52(5): 1000–1015.

Yamashita, K., Tanikawa, T., Shigeno, Y. & Hamada, J. 2015. Vertical load sharing of piled raft with grid-form deep mixing walls. *Conference on Deep Mixing 2015*, San Francisco, 437–446.

Yamashita, K., Hamada, J. & Tanikawa, T. 2016. Static and seismic performance of a friction piled combined with grid-form deep mixing walls in soft ground. *Soils & Foundations* 56(3): 559–573.

Yamashita, K., Shigeno, Y. Hamada, J. & Chang, D. W. 2018. Seismic response analysis of piled raft with grid-form deep mixing walls under strong earthquakes with performance-based design concerns, *Soils & Foundations* 58(1): 65–84.